Influence of Tin Additions on the Phase-Transformation Characteristics of Mechanical Alloyed Cu-Al-Ni Shape-Memory Alloy

SAFAA N. SAUD, E. HAMZAH, T. ABUBAKAR, H.R. BAKHSHESHI-RAD, and M.N. MOHAMMED

The influence of the addition of Sn to Cu-Al-Ni alloy as a fourth element with different percentages of 0.5, 1.0, and 1.5 wt pct on the microstructure, phase-transformation temperatures, mechanical properties, and corrosion behaviors was investigated. The modified and unmodified alloys were fabricated by mechanical alloying followed by microwave sintering. The sintered and homogenized alloys of Cu-Al-Ni-xSn shape-memory alloys had a refined particle structure with an average particle size of 40 to 50 μm associated with an improvement in the mechanical properties and corrosion resistance. With the addition of Sn, the porosity density tends to decrease, which can also lead to improvements in the properties of the modified alloys. The minimum porosity percentage was observed in the Cu-Al-Ni-1.0 wt pct Sn alloy, which resulted in enhancing the ductility, strain recovery, and corrosion resistance. Further increasing the Sn addition to 1.5 wt pct, the strength of the alloy increased because the highest volume fraction of precipitates was formed. Regarding the corrosion behavior, addition of Sn up to 1 wt pct increased the corrosion resistance of the base SMA from 2.97 to 19.20 kΩ cm^2 because of formation of a protective film that contains hydrated tin oxyhydroxide, aluminum dihydroxychloride, and copper chloride on the alloy. However, further addition of Sn reduced the corrosion resistance.

I. INTRODUCTION

BECAUSE of the unique properties of pseudoelasticity, shape-memory effect, and damping capability, Cu-based shape-memory alloys (SMAs) have been widely utilized in numerous practical applications.[1,2] The binary systems of Cu-Zn and Cu-Al are the two primary copper-based alloys that operate in the areas of the β-phase. Undoubtedly, Cu-Al-Ni SMAs are the most-employed alloys when high temperatures are needed.[3] For this reason, they can be used at high transformation temperatures, which are able to work at or perhaps close to 473 K (200 °C),[4] which is usually difficult for Cu-Zn-Al and Ni-Ti alloys,[5,6] whose maximum temperatures are approximately 373 K (100 °C).[7] The incorporation of a fourth element, for instance, Ti, Zr, Mn, B, Y, or V and rare earths into the ternary Cu-Al-Ni SMAs as a grain refiner may lead to microstructural adjustments in the phase formation, types, and distribution, oppositely to enhance the mechanical

properties of conventionally cast Cu-Al-Ni SMA alloys.[8–11] However, a minor addition was demonstrated to be ineffective in controlling grain growth to an adequate level, while excessive addition tended to change the chemical composition of the alloy, and therefore shift the transformation temperature.[12] Moreover, excessive addition of the alloying element can also form a high volume fraction of precipitates (second-phase particles), which may also affect the mechanical properties.[13]

The main issues are to prevent high brittleness in the conventional casting of the ternary and quaternary Cu-Al-Ni alloys and produce a large grain size associated with a high elastic anisotropy, which are categorized as major prohibitive factors that limit their commercial applications.[14–16] In addition, the casting process usually leads to a change in the chemical composition of the alloy, which may cause a shift in the transformation temperatures.[17] Therefore, alternative processing routes that have the ability to control grain size and composition, mechanical alloying (MA) as a powder metallurgy process, were developed.[4,18] These processes are solid-state powder techniques that are widely used to produce refractory metals, dispersion-strengthen alloys, nanocrystalline, and amorphous composite materials.[19–21] A number of researchers have studied the transformation characteristics of Cu-Al-Ni produced by PM, and then sintered using different kinds of sintering techniques.[3,4,13,22–24] Most of these techniques have disadvantages, including being time-consuming, the presence of a high percentage of porosity/cracks, and thus reduction in the mechanical properties.

SAFAA N. SAUD and M.N. MOHAMMED, Senior Lecturers, are with the Faculty of Information Science and Engineering, Management and Science University, 40100 Shah Alam, Malaysia, and also with the Faculty of Mechanical Engineering, Universiti Teknologi Malaysia, 81310 UTM Johor Bahru, Johor, Malaysia. Contact e-mail: safaaengineer@gmail.com E. HAMZAH, Professor, and H.R. BAKHSHESHI-RAD and T. ABUBAKAR, Senior Lecturers, are with the Faculty of Mechanical Engineering, Universiti Teknologi Malaysia.

Microwave sintering involves a new sintering routine used to heat the green compacts nearly to sintering temperature for densifying and alloying the metals, ceramics, and composites. It is able to incorporate the prealloyed elements using microwaves and volumetrically absorb the electromagnetic energy, and then transform it into heat.[25–27] In contrast to the typical sintering methods, the microwave sintering approach demonstrates several fundamental features, minimized energy intake, rapid heating rates, minimized sintering times, improved element diffusion processes, and enhanced physical and mechanical properties.[25]

So far, an appropriate and systematic study of the Tin addition on the phase transformation and shape-memory properties of Cu-Al-Ni SMA has not been performed. Thus, in this research, the prealloyed powders of Cu, Al, Ni, and Sn were prepared using high-energy planetary ball milling, compacted, and then sintered using microwave sintering to obtain the final alloy. The aim of the research is to investigate the effect of different amounts of Sn addition on the microstructure, mechanical properties, and corrosion characteristics of Cu-Al-Ni SMAs.

II. EXPERIMENTAL PROCEDURE

In this research, the elemental powders of Cu, Al, and Ni, with Sn as an additional element, were prepared by mechanical alloying. The specifications of the elemental powder and initial powder mixtures are shown in Table I. The mechanical alloying experiments were conducted on a Retsch PM100 planetary ball mill using zirconium oxide vial and balls for 1 hour to assure the homogeneity of the powder. The rotation speed of the ball mill was 300 rpm and ball-to-powder ratio was about 5:1 by weight. The process was carried out at an evacuated condition at the room temperature and an argon gas was used to avoid the oxidation of powders.

The prealloyed powder was hot pressed into green samples with dimensions of ϕ 15 × 10 mm^2 for the microstructural characterization and ϕ 15 mm × (L) 30 mm for the mechanical test through a 10-ton hand-operated hydraulic press and a single-act piston die of 15 mm diameter was utilized. The compaction process was carried out at a constant temperature of 573 K (300 °C) for 10 minutes; the temperature was maintained via an external heater tape connected to a thermoset to set the exact temperature. The green samples were placed into a 2.45 GHz, 0.3 to 3.0 kW consistently flexible microwave device (HAMiLab-V3, SYNOTHERM Corp.). The green samples were inserted inside an alumina sagger and covered with silicon carbide (SiC). The function of SiC is usually to function as a microwave susceptor to

enable the heating system and also sintering of the green samples. The samples were sintered by microwave heating at a rate of 20 °C/min to 1173 K (900 °C) for 30 minutes. Argon gas with a purity of 99.995 pct was pumped into the microwave chamber throughout the sintering with the intent to protect against oxidation. To measure the temperature of all samples through the sintering, a Reytek IR pyrometer was utilized. Prior to the microstructure characterization, the sintered samples were homogenized at 1173 K (900 °C) for 30 minutes and directly quenched in water.

The green porosity was calculated using the following equation:[28,29]

$$P = \left\{ 1 - \left(\frac{\rho_g}{\rho_{th}} \right) \right\} \times 100 \text{ pct}, \qquad [1]$$

where ρ_g is the green density and can be calculated by division of the calculated weight by the measured volume; ρ_{th} is the theoretical density of the samples and can be calculated as follows:

$$\rho_{th} = \begin{bmatrix} \rho_0^{Cu} \times (\text{at. pct Cu}) + \rho_0^{Al} \times (\text{at. pct Al}) + \rho_0^{Ni} \\ \times (\text{at. pct Ni}) + \rho_0^{Oxy} \times (\text{at. pct Oxy}) + \rho_0^{additives} \\ \times (\text{at. pct additives}) \end{bmatrix},$$

$$[2]$$

where ρ_0^{Cu}, ρ_0^{Al}, ρ_0^{Ni}, ρ_0^{Oxy}, and $\rho_0^{additives}$ are the theoretical densities of the base-alloy elements and additives.

The microstructure changes of the prealloyed and homogenized samples were investigated using a field-emission–scanning electron microscope (FE–SEM), Zeiss-LEO Model 1530 operated at 10 kV coupled with energy-dispersive spectroscopy (EDS) operated at 5 kV. The results of EDS were indicated in accordance with a standardless semiquantitative analysis and an error bar in value of 5 pct was added to each reading. The microstructural features of the Cu-Al-Ni SMA with and without addition were also studied with a transmission electron microscope (TEM) operating at 120 kV. The phase and crystal structure were identified using a D5000 Siemens X-ray diffractometer fitted with a Cu Kα X-ray source with a locked coupled mode, a 2θ range between 30 and 80 deg, and a 0.05 deg/s scanning step. Based on the Williamson–Hall method,[30] the crystallite size and microstrain were determined using the following equation:

$$\frac{\beta}{2} \cot \theta = \frac{0.45\lambda}{\sin \theta \times D} + \varepsilon, \qquad [3]$$

where β is the diffraction peak width at midheight, λ is the X-ray wavelength, D is the average crystallite size (nm), ε is the microstrain, and θ is the Bragg diffraction

Table I. Specification of Elemental Powders and Mixture

Properties	Cu	Al	Ni	Sn
Size (μm)	150	25	45	45
Purity (pct)	99.999	99.99	99.95	99.9
Composition (wt pct)	83.5−x	12.5	4	x (0.5,1.0, and 1.5)

angle. The transformation temperatures of the mechanically alloyed Cu-Al-Ni alloy specimens with and without addition were evaluated via differential scanning calorimetry (DSC) at a heating/cooling rate of 10 °C/min.

The mechanical properties of the Cu-Al-Ni alloys with and without addition were evaluated by performing compression tests on the specimens in the martensitic state, wherein subsize test specimens with the dimension of ϕ 15 mm × (L) 30 mm were prepared. The compression tests were carried out on an Instron 5982-type universal testing machine at an extension rate of 0.5 mm/min. To measure the shape-memory recovery of the alloys, the compressive loading and unloading were carried out at a tested temperature of 473 K (200 °C) and an isothermal compression test was performed.

Rectangular specimens with a surface area of 1 cm^2 were prepared for potentiodynamic polarization (PDP) tests. PDP was performed in an open-air glass cell containing 350 mL of 3.5 wt pct NaCl solution using a potentiostat (PARSTAT 2263 Princeton Applied Research). A three-electrode cell was used for the PDP tests, where a saturated calomel electrode (SCE) was used as the reference electrode, a graphite rod as the counter electrode, and an alloy specimen as the working electrode. The samples were immersed in the simulated body fluid (SBF) for 1 hours prior to the PDP test to establish the open-circuit potential. PDP experiments ($n = 2$) were conducted at a constant scan rate of 0.5 mV/s, and initiated at −250 mV below the open-circuit potential. Immersion testing was carried out according to ASTM G1-03. Specimens with a diameter of 10 mm and thickness of 10 mm were immersed in a beaker containing 200 mL of 3.5 wt pct NaCl solution for 30 days. The immersion tests were repeated at least once to verify the reproducibility of the results.

III. RESULTS AND DISCUSSION

A. Effect of Sn Addition on the Porosity

The variation of green density and porosity of the modified and unmodified alloys as a function of the Sn amount are shown in Figure 1. It can be clearly seen that the addition of Sn has produced a significant effect on the porosity density, in which the addition of 1 wt pct Sn led to an increase in the green density from 5.35 to 6.65 g/cm^3, while the green porosity was reduced from 12.96 to 4.81 pct. This may be attributed to the lower melting temperature of Sn during sintering process which leads to closing of more pores in comparison with Cu and Ni which have a melting point higher than the sintering temperature.[31,32] With further increase in the Sn amount to 1.5 wt pct, the green density decreased and green porosity increased. This decrement is mainly because of the excess of the solid solubility of Sn addition in the base alloy, i.e., >1.3 wt pct.[33]

B. Microstructural Investigation

Figure 2 shows micrographs of prealloyed and homogenized Cu-Al-Ni SMAs associated with the
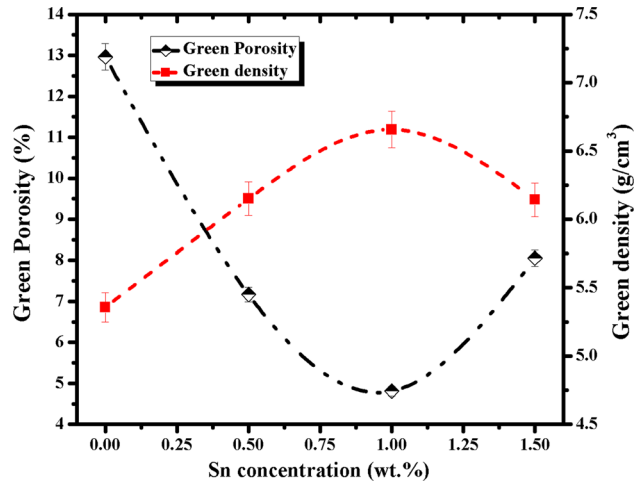

Fig. 1—Green density and porosity of the alloys as a function of Sn amount.

chemical analysis of the homogenized samples. From the morphology of prealloyed samples, neck formation between the powder particles can be easily seen; these necks are caused by the cold working of the element powder that occurred during the mechanical alloying (ball-milling process). The morphology of the MA powders and the microstructure bulk alloys after sintering and homogenization are shown in Figure 2. It was found that the bulk alloys contain some semimicron sized pores. Although these pores were distributed randomly in the microstructure, they most likely lie along the particle boundaries after the sintering and homogenization processes. Furthermore, after the addition of Sn with different percentages, the density of these pores tends to decrease with increasing amount of Sn up to 1 wt pct; however, with further Sn addition to 1.5 wt pct, the pore density was slightly increased. It was also observed that the particle size of MA powders was about 40 to 50 μm, both before and after addition. This kind of reduction is mainly related to the effect of mechanical alloying. In general, the particle size of Cu-Al-Ni SMA that is produced by conventional casting was determined to be 300 to 1400 μm,[8,12,34] even though the alloying elements and thermal treatments were applied.

After homogenization at 1173 K (900 °C), the analyzed chemical compositions of the Cu-Al-Ni-xSn alloys were examined using EDS and are shown in Figure 2. It was found that the ratio of elemental Sn in different amounts of addition was slightly changed compared with the nominal composition. Furthermore, the percentage of oxygen was found to decrease after the addition of Sn and homogenization. Homogenization of the Cu-Al-Ni alloys at temperatures in the β-phase field followed by rapid cooling produces microstructures formed by metastable phases, which can result in martensitic transformation.

From the FE–SEM high-resolution images (Figure 2), it can be seen that there are two phases with different morphologies, plate-like and needle-like, with a self-accommodating configuration inside the merged particles.
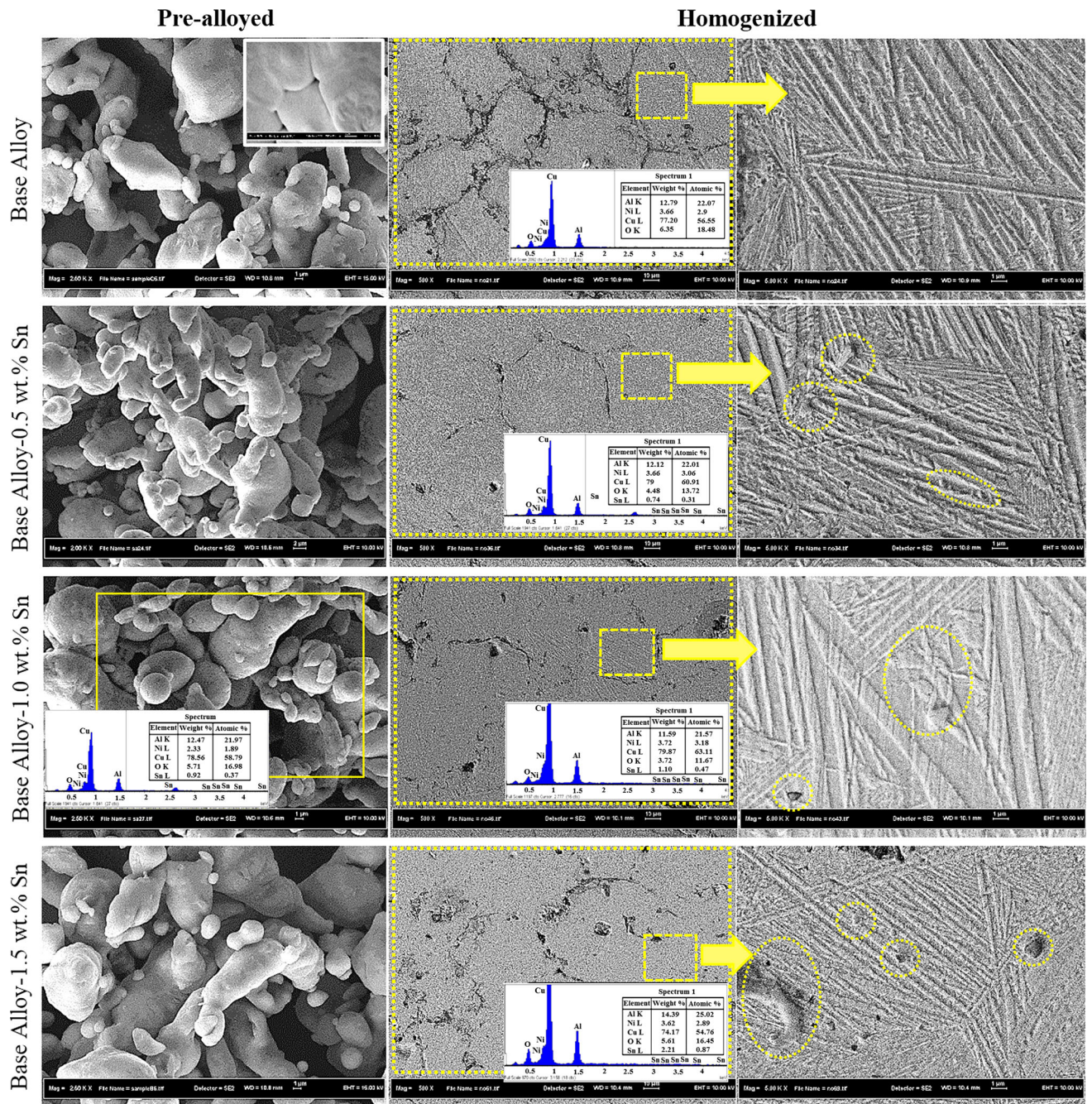
Pre-alloyed   **Homogenized**

Fig. 2—Micrographs of the prealloyed and homogenized Cu-Al-Ni-xSn SMAs along with EDS.

These phases are β_1' and γ_1', which are formed as thermally induced martensites, and varied in terms of thickness and orientation after the addition of Sn, as shown in Figure 2. The γ_1' phase formed as a coarse variants/plate-like phase, while the β_1' phase formed as a needle-like phase between the γ_1' phases. The needle-like phase of β_1' martensite has a very high thermoelastic behavior, which can be attributed to its controlled growth in the self-accommodating groups.[35–37] However, when Sn was added, new phases were formed and the volume fraction of these precipitates varied

according to the amount of Sn added. It is well known that tin is an attractive element that causes formation of precipitates after addition.[38] These precipitates are able to form in the Cu/Ni matrix and thus, the formation of β_1' martensite is promoted;[12] in addition, they are also have the ability to accommodate the γ_1' and β_1' parent phases, and their accommodation is in a coherent or mostly semicoherent mode that depends on the precipitates' sizes and crystal-structure orientations relative to the parent phase.[39] When the matrix surrounding one precipitate is transformed to a single variant of
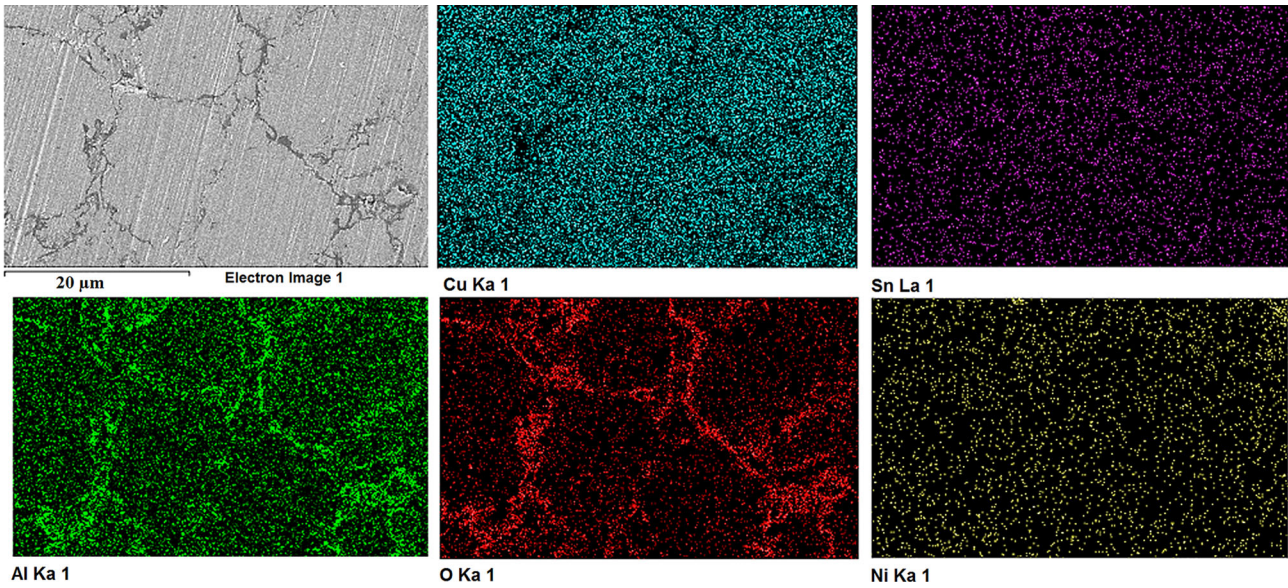
Fig. 3—Elemental mapping of the homogenized Cu-Al-Ni-1 wt pctSn SMA.
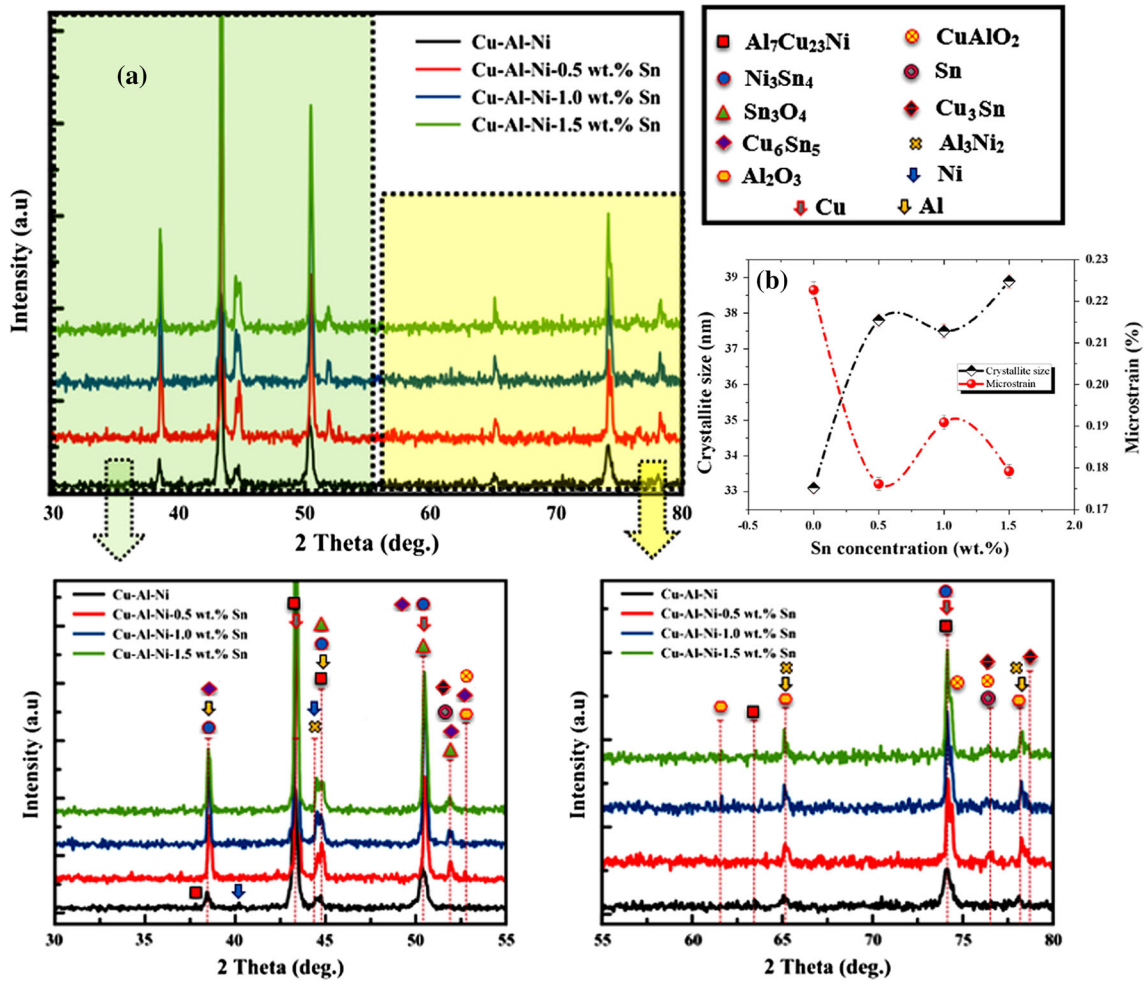

Fig. 4—(a) XRD diffraction patterns of the homogenized Cu-Al-Ni-xSn SMAs, (b) Crystallite size and microstrain of the samples as a function of Sn concentration.

Table II. Crystallite Size, Microstrain, and Lattice Parameters of the Homogenized Cu-Al-Ni-xSn SMAs

Alloy	Lattice Parameters				Crystallite Size (nm)	Microstrain (pct)
	a (Å)	b (Å)	c (Å)	β		
Cu-Al-Ni	3.55	6.16	37.59	90.9	33.1	0.22
Cu-Al-Ni-0.5wt pct Sn	3.72	8.32	41.54	94.27	37.8	0.17
Cu-Al-Ni-1.0wt pct Sn	3.68	8.34	41.19	93.43	37.5	0.17
Cu-Al-Ni-1.5wt pct Sn	3.71	8.33	41.46	93.98	38.9	0.19

Table III. Volume Fraction of Parent Phases and Precipitates in the Homogenized Cu-Al-Ni-xSn SMAs

Alloy	Volume Fraction (pct)											
	Cu	Al	Ni	Sn	$Al_7Cu_{23}Ni$	Ni_3Sn_4	Sn_3O_4	Cu_6Sn_5	Al_2O_3	$CuAlO_2$	Cu_3Sn	Al_3Ni_2
Cu-Al-Ni	40.55	3.43	3.55	—	32.24	—	—	—	5	11.85	—	3.38
Cu-Al-Ni-0.5wt pct Sn	37.22	7.48	—	0.64	21.51	8.57	10.31	1.84	2.50	6.99	2.01	—
Cu-Al-Ni-1.0wt pct Sn	22.33	4.98	—	1.25	17.45	7.7	14.8	1.98	3.33	4.98	2.40	—
Cu-Al-Ni-1.5wt pct Sn	30.1	5.67	—	1.35	23.38	12.15	29.58	2.08	6.75	5.97	2.70	—

martensite, the hole left in the β matrix occupied by the precipitate is quite severely deformed due to the intrinsic deformation accompanying the transformation,[40] but the precipitate itself maintains its shape. Therefore, the microstructure, and hence the mechanical behavior of Cu-Al-Ni alloys, changes with the alloy composition and the processing routes to which the samples are subjected. The elemental mapping of the homogenized Cu-Al-Ni-1 wt pct Sn SMA is presented in Figure 3. It is worth mentioning that the alloy elements were distributed homogeneously in the microstructure, except for Al element, which was mostly agglomerated/segregated at the particle boundaries after reacting with oxygen, as shown in Figures 3(c) and (d).

The XRD patterns of the homogenized Cu-Al-Ni-xSn SMAs with different percentages of Sn are potentially presented in Figure 4. Indexing of these patterns shows that these only consist of martensite phases γ_1' (orthorhombic structure) and β_1' (monoclinic structure) along with some other precipitates/intermetallic compounds that are also formed after being homogenized at 1173 K (900 °C) for 1 hour. After the addition of Sn, the scanned peaks changed in terms of 2θ and intensity, which shows that the XRD patterns of Cu-Al-Ni SMA are sensitive to the amount of added Sn. On the other hand, the matrix of Cu-Al-Ni SMA as the predominant phase was always retained, even though Sn amounts varied. Further increasing the amount of Sn, *i.e.*, 1.5 wt pct, the XRD results also show that the intensity for the compounds and precipitates of Ni_3Sn_4, Sn_3O_4, Al_2O_3, Cu_6Sn_5, and Cu_3Sn increased, while the intensity of $Al_7Cu_{23}Ni$, $CuAlO_2$, and Al_3Ni_2 decreased. This increment in the volume fraction of these precipitates after 1.5 wt pct Sn addition is mainly attributed to the high amount of Sn, which has exceeded the solubility limit of Sn (*i.e.*, 1.3 wt pct) in accordance with the phase diagram of the Cu-Sn system.[41] On the other hand, with Sn content increasing, the volume fraction of the γ_1' phase decreases, which is shown by the decreasing intensity of the peaks of the γ_1' phase in the alloy

containing 1.5 wt pct Sn. According to the XRD patterns of the Cu-Al-Ni SMA (Figure 4), by adding different amounts of Sn, the main peaks underwent a positional shift toward higher values of 2θ because of the substitution of Sn atoms in Cu sites in the alloy lattice. As observed in Table II, the *a*-axis, *b*-axis, and *c*-axis values increased in the modified samples compared with the values of the unmodified sample. This increase in the lattice parameters of the Cu-Al-Ni SMA may be attributed to the Sn being more massive and larger than Cu, which caused a distortion in the copper lattice in the neighborhood of the atom during the addition.[42,43] Moreover, it was also found that the distortion in the Cu sites during addition, sintering, and/or homogenization affected the fraction of the crystalline size and microstrain of the parent phases. To examine the effect of Sn addition on the crystallite size of the base alloy (Cu-Al-Ni), XRD profiles were used to evaluate the crystallite size of the modified and unmodified alloys. As observed in Figure 4(b) and Table II, the increase in lattice parameters of the base alloy because of the dissolution of more Sn atoms in the alloy lattice during addition and homogenization caused the crystallite size of the homogenized alloys to increase gradually from 33.1 nm in the base-alloy sample to 38.9 nm in the modified alloy with 1.5 wt pct Sn addition; however, the microstrain decreased from 0.22 to 0.17 pct with Sn addition. The changes in crystallite size and microstrain of Cu-Al-Ni SMA as a function of Sn amount are shown in Figure 4(b). In addition, the gradual increase in the crystallite size of the base alloy was shown by the broadening and increases in the intensity of the base-alloy XRD peaks after being modified with 1.5 wt pct Sn. A possible interpretation of these changes is that the addition of Sn has reduced the evolving stresses during the PM, and thus, the crystallite size increased while the microstrain decreased with increasing Sn amounts.

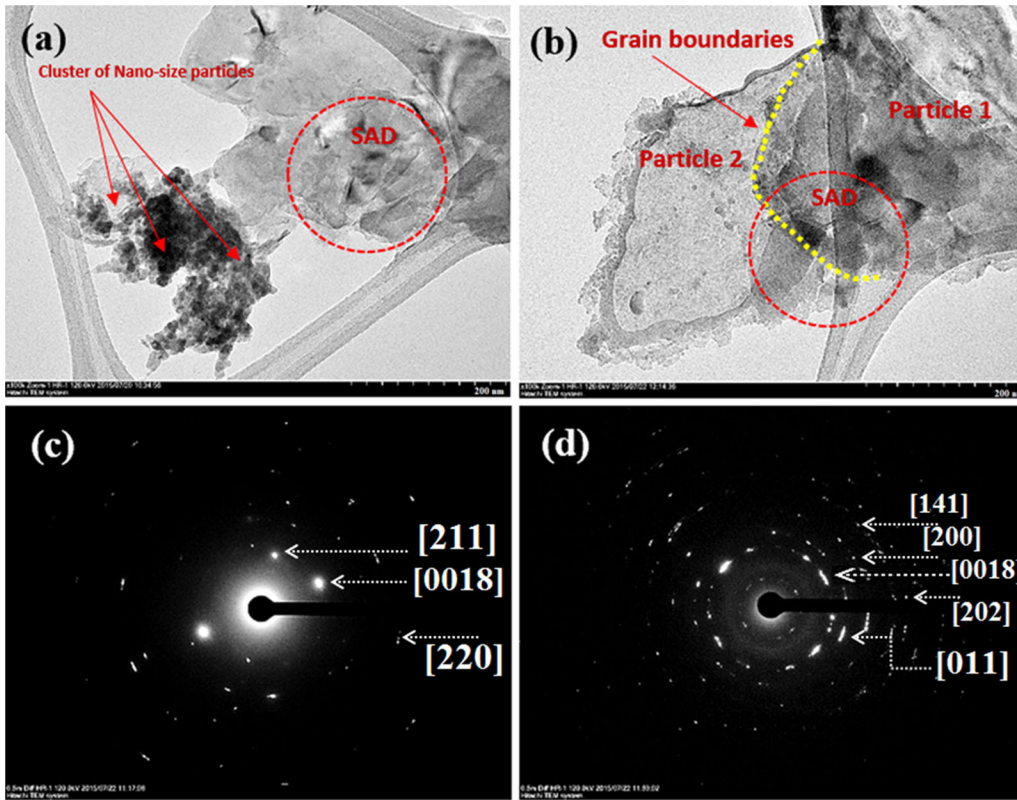The volume fractions (R_X pct) of the raw elements together with produced phases for modified and

Fig. 5—TEM micrographs correspond with the SAED of the prealloyed, (*a, c*) Cu-Al-Ni SMA, (*b,d*) Cu-Al-Ni-1Sn SMA.
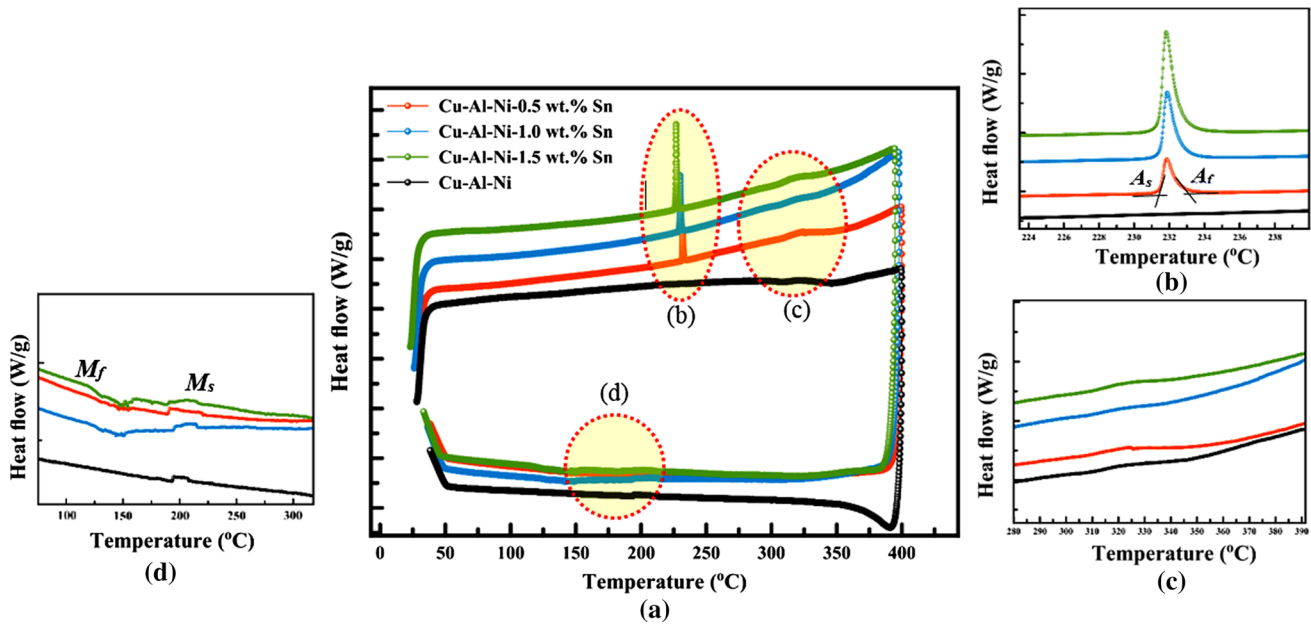

Fig. 6—DSC curves of the homogenized Cu-Al-Ni-*x*Sn SMA (*a*) full scan, (*b, c*) heating, and (*d*) cooling.

unmodified alloys were computed and the data are tabulated in Table III. In accordance with the dependence of the diffracted intensity on the absorption coefficient of the mixture and because the intensity of the XRD peaks changes with concentration, a linear relationship between the intensity and concentration does not take place. Consequently, the area under the peak is proportional to the volume fraction of the

concentration, and this can be determined from the following equation:

$$R_X = \frac{a_X}{\sum a_i},\qquad [4]$$

where R is the volume fraction, X is elemental/intermetallic compounds of the homogenized alloys, a_X is the related area of the elemental/compounds peaks, and $\sum a_i$ is the total area of the observed peaks. It was found that $R_{Al7Cu23Ni}$ decreased as Sn increased; this may be attributed to the decreases of intensity of the observed peaks in the XRD patterns, and thus decrease in the area under the peaks that expressed the value for this phase. On the other hand, the volume fraction of overall precipitates (Ni_3Sn_4, Sn_3O_4, Al_2O_3, Cu_6Sn_5, and Cu_3Sn) increased considerably in the modified alloys. This increase implies that the precipitates turned out to be more stable, so that a certain amount of the Sn phase formed into the product phases.[44]

A detailed study of the prealloyed powders was performed using TEM by analyzing a significant number of particles. The morphological shape and size of the powder mixture of the base-alloy samples with and without the addition of 1.0 wt pct Sn obtained from TEM are shown in Figure 5. In the base-alloy samples, the powders were taken as polygonal-shaped particles and the fringe lattices are clearly observed, where they have been oriented in different directions and d-spacing in accordance with the present phases after being milled for 1 hour at 300 rpm. Furthermore, it was found that there are some clusters of nanosize particles with a size range of 5 to 25 nm agglomerated at the boundaries of the particles. In the modified alloy of Cu-Al-Ni SMA with 1.0 wt pct (Cu-Al-Ni-1Sn), the particle boundaries have been converted to particle boundaries, which show as yellow dots in Figure 5(b). However, in this alloy, the agglomerated particles have been distributed on the inside and boundaries of the particles, as clearly demonstrated in particle 2 in Figure 5(b). Based on the results of the corresponding selected area electron diffraction (SAED), it was found that the degree of crystallinity of the Cu-Al-Ni SMA has been increased

Fig. 7—Stress–strain compressive curves of Cu-Al-Ni-xSn SMA.

with the addition of Sn in Figures 5(c) and (d), which is in good agreement with the XRD results in Table II.

C. Transformation Temperatures

Figure 6 shows the exothermic and endothermic curves of the Cu-Al-Ni-xSn SMAs, where x is 0.5, 1.0, and 1.5 wt pct. The peak temperatures including forward austenitic transformation start temperatures (A_s), forward austenitic transformation finish temperatures (A_f), reverse martensitic transformation start temperatures (M_s), and reverse martensitic transformation finish temperatures (M_f) appearing in Figures 6(a) and (b). It was found that the DSC curves of the modified and unmodified Cu-Al-Ni SMA with Sn show almost identical behavior during the heating and cooling processes. In the modified alloy, a very sharp peak was observed at 505 K (232 °C) in addition to the broad peak at 623 K (350 °C), where this peak may be related to the presence of precipitates of Cu, Ni, and Sn as a result of the formation of Sn, which limits the stability of the low-temperature phase[7,45] and causes an individual transformation because of a greater driving force. During the transformation, thermal exchange between the base phase and the formed martensite phases provides the driving force, thus shifting the transformation temperatures. Furthermore, the forward MT shows two peaks, and this behavior features the transformation $\beta \rightarrow \beta' + \gamma'$;[45,46] however, their presence is due to the different hystereses of both transformations.

On the cooling curves, very small multipeaks were observed, which mainly correspond to the established intermetallic compounds' transformation through the transformation of austenite to martensite.[34,47] The observation of these multipeaks was not as clear as compared with the forward transformation, which may be related to insufficient heat transfer required for the formation and transformation of the martensite phase.[22] A number of the modified alloys have shown multiple endothermic/exothermic peaks in their transformation curves; their multiple peaks are attributed to the interface transformations. These intermartensitic transformations are a first-order phase transformation between martensites with different structures at temperatures below the Ms. So far, several intermartensitic phases have been found in the shape-memory alloys, which have modulated a lattice with a different periodicity of stacking sequences.[48] However, the structures and transformation temperatures of these intermartensitic phases depend on the levels of applied stress and the chemical composition. On the other hand, these interphases are very sensitive to the internal stress of the alloy.[49] Finally, it must be highlighted that the present homogenized alloys have high representative transformation temperatures, which make these alloys more suitable for high-temperature applications.

D. Mechanical Properties and Shape-Memory Characteristics

Figure 7 shows a typical stress–strain curve for the homogenized Cu-Al-Ni SMA before and after addition
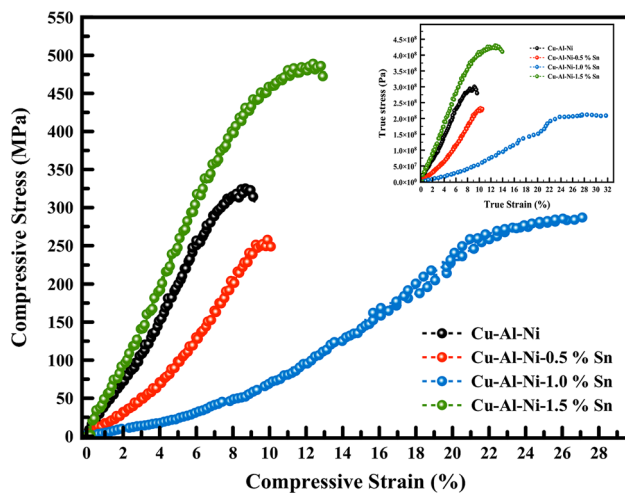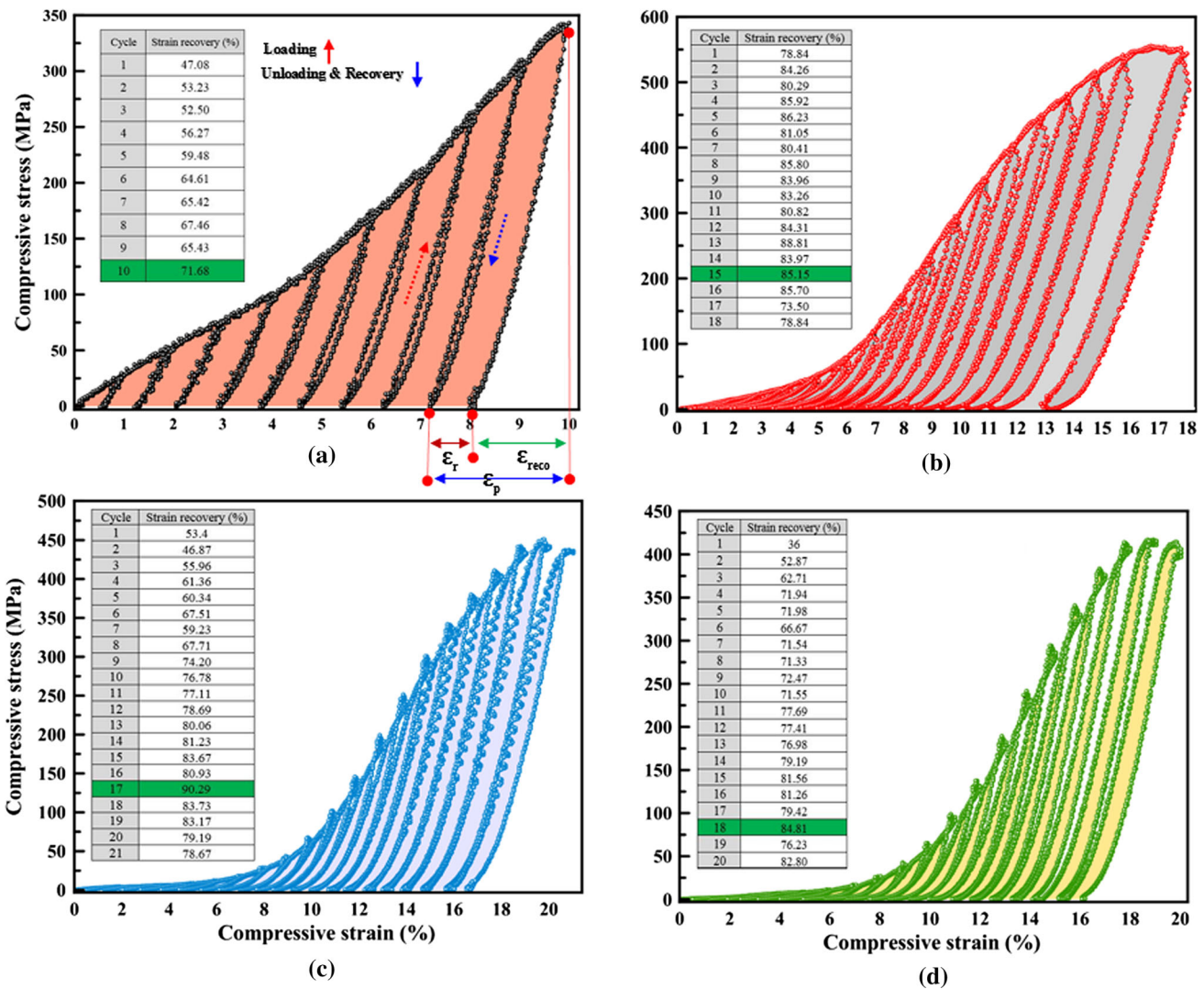
Fig. 8—Compressive stress–strain of different loading–unloading cycles tested at a temperature of 473 K (200 °C); (a) Cu-Al-Ni; (b) Cu-Al-Ni-0.5 wt pct Sn; (c) Cu-Al-Ni-1.0 wt pct Sn; and (d) Cu-Al-Ni-1.5 wt pct Sn.

of Sn that performed at the room temperature. The compressive strength of the base alloy (Cu-Al-Ni) gave the shape of "S" variations with Sn addition, namely with increasing the amount of Sn, the strength decreased initially, and then increased with increasing amount of Sn to 1.5 wt pct. The compressive strength and strain were in the range of 247.75 to 472.49 MPa and 8.96 to 27 pct, respectively. These variations are mainly attributed to the different volume fraction of the γ'_1 phase and/or precipitates associated with the reducing porosity density after the addition of Sn. In general, the volume fraction and size of precipitates have an adverse effect on the mechanical properties of shape-memory materials.[50,51] It was found that the highest volume fraction of precipitates was with the addition of 1.5 wt pct of Sn, which may let the precipitates act as obstacles to the movement of dislocation/phase interfaces, which makes the martensite transformation more difficult during the deformation process.[52,53]

To investigate the shape-recovery behavior of the modified Cu-Al-Ni SMA, a cyclic loading–unloading compression test was carried out. Figure 8 shows the stress–strain curves of Cu-Al-Ni SMA with and without addition tested at a temperature of 200 °C. The broken red and blue dot arrows drawn in the figure indicate loading and unloading/recovery, respectively. The strain recovery, ε_r, was defined as the difference between the plastic strains of the alloys and the residual strain that occurred after the recovery cycle was completed. It was found that the largest number of cycles was indicated with the Cu-Al-Ni-1Sn SMA before the occurrence of fracture. This improvement is due to two reasons: low porosity density and the finest particle size among the alloys. According to the strain-recovery calculation for different cycles, it was found that the strain recovery of the alloys varied from the first cycle until the cycle before fracture because of the inconsistency of thermoelastic martensite.[54] The largest strain recovery of 90.29 pct was found with the Cu-Al-Ni-1Sn, indicating that this alloy exhibits a good resistance to irreversible martensite stabilization during the test, and the following implication
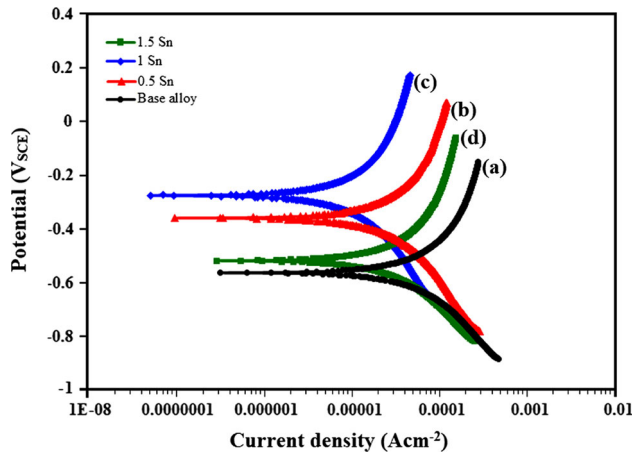
Fig. 9—PDP curves of specimens in 3.5 wt pct NaCl solution (*a*) Cu-Al-Ni, and Cu-Al-Ni-Sn SMAs with various Sn contents: (*b*) 0.5, (*c*) 1, and (*d*) 1.5 wt pct.

of Cu-Al-Ni-1Sn > Cu-Al-Ni-0.5Sn > Cu-Al-Ni-1.5Sn > Cu-Al-Ni was noted. The main reasons behind the enhancement of the shape recovery are the formation of various kinds of precipitates, a minimum of the porosity density along with variations in the volume fraction and size of the γ'_1 and β'_1 parent phases, which have a detrimental influence on the shape-memory recovery.[22,34,51,55,56] In the shape-memory alloys produced by MA/PM, the shape-memory recovery depends on the microstructure of the alloy and the martensite stabilization. However, the occurrence of cracks and stress concentrations around the pores may lead to a rapid degradation in the shape-memory alloys.[57,58] In this research, the microwave sintering reduces the density/presence of porosity; therefore, the produced alloys have exhibited a very good shape-memory recovery.

E. Electrochemical Measurements

The polarization curves for ternary Cu-Al-Ni and quaternary Cu-Al-Ni-Sn SMAs in 3.5 wt pct NaCl solution are shown in Figure 9. The corrosion potential (E_{corr}) of Cu-Al-Ni SMA is −560.6 mV$_{SCE}$, while the E_{corr} of the Cu-Al-Ni-0.5Sn SMA alloy lies at −357.6 mV$_{SCE}$. The E_{corr} was ennobled by about 287.3 and 45.1 mV$_{SCE}$ because of 1 and 1.5 wt pct tin addition to Cu-Al-Ni SMA (Table IV). The more positive E_{corr} of SMA containing 1 wt pct Sn is due to formation of a complex oxide film of tin, aluminum, and copper compounds, including chlorides, but in low amount.[59]

From the i_{corr} comparison between the ternary and quaternary SMAs, it can be inferred that Cu-Al-Ni-1Sn SMA exhibited the most favorable corrosion behavior as a result of its consistently low corrosion rate in corrosive media. However, ternary and the other quaternary SMA alloys, such as Cu-Al-Ni-0.5 wt pct Sn SMA, demonstrated low i_{corr} in electrolyte, and the i_{corr} of the ternary Cu-Al-Ni SMA is lowest. In general, the lower the corrosion current density, the lower the

Table IV. Electrochemical Parameters of Ternary Cu-Al-Ni and Quaternary Cu-Al-Ni-Sn SMAs in 3.5 wt pct NaCl Solution Obtained from the Polarization Test

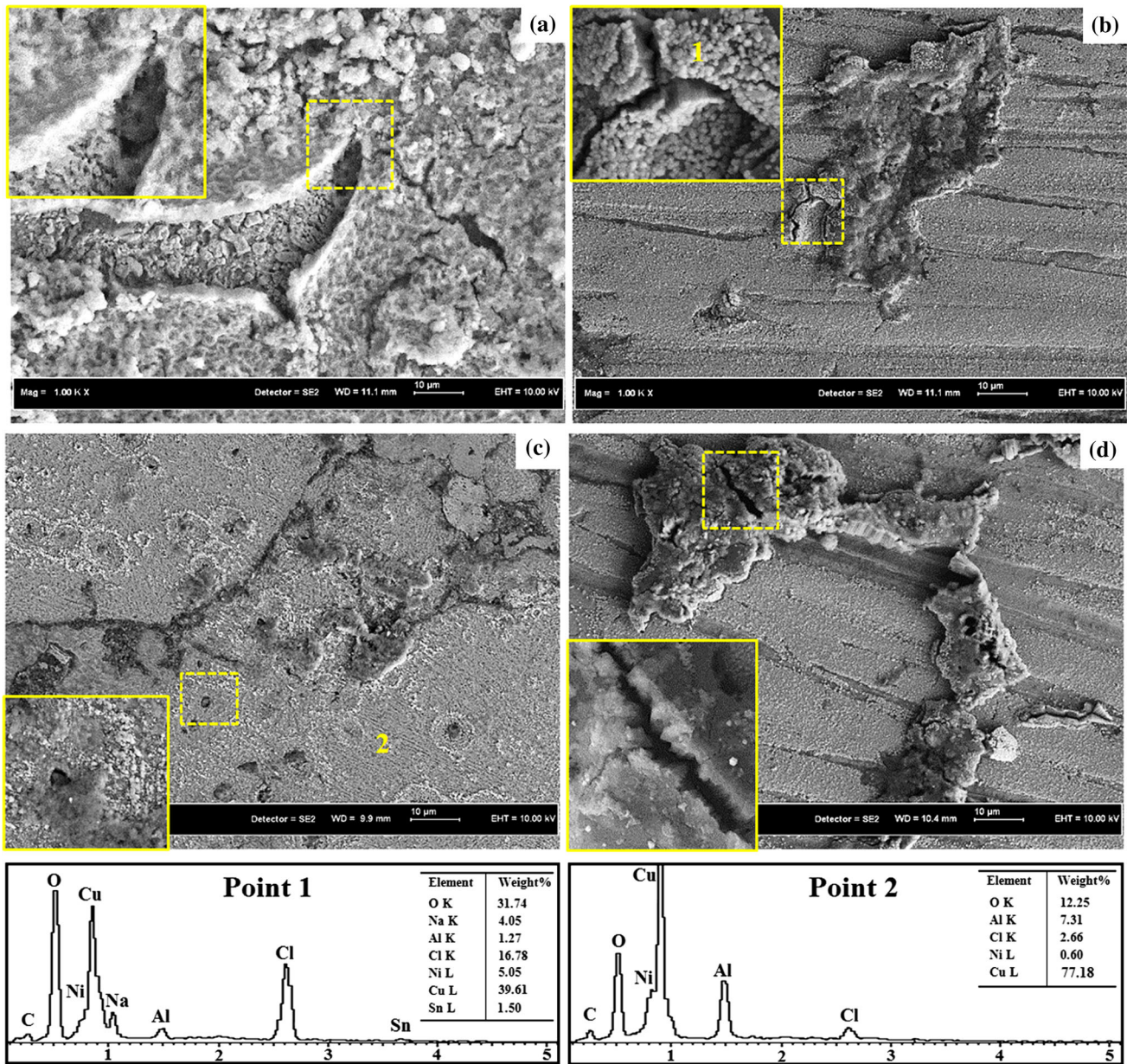| Alloy	Corrosion Potential, E_{corr} (mV vs SCE)	Current Density, i_{corr} ($\mu A/cm^2$)	Cathodic Slope, β_C (mV/decade) vs SCE	Anodic Slope, β_a (mV/decade) vs SCE	Polarization Resistance, R_P (kΩcm^2)	Corrosion rate, P_i (mm/year)
Cu-Al-Ni	−560.6	139.8	176	210	2.97	3.19
Cu-Al-Ni-0.5 wt pct Sn	−357.6	94.8	212	250	5.26	2.16
Cu-Al-Ni-1 wt pct Sn	−273.3	27.3	225	260	19.20	0.62
Cu-Al-Ni-1.5 wt pct Sn	−515.5	112.1	198	240	4.20	2.56

Fig. 10—SEM micrographs of (*a*) Cu-Al-Ni and Cu-Al-Ni-Sn SMAs with various Sn contents: (*b*) 0.5, (*c*) 1, and (*d*) 1.5 wt pct and corresponding EDS analyses of Points 1 and 2 after immersion in 3.5 wt pct NaCl for 30 days.

corrosion rate. The i_{corr} can be ranked in the following order: Cu-Al-Ni < Cu-Al-Ni-1Sn < Cu-Al-Ni-0.5Sn < Cu-Al-Ni-1.5Sn. The corrosion current density, i_{corr}, is related to the corrosion rate, R_i by the following equation:[60,61]

$$R_i = 22.85 i_{corr}. \qquad [5]$$

Samples Cu-Al-Ni-0.5wt pct Sn and Cu-Al-Ni-1wt pctSn SMAs demonstrated the lowest corrosion rates (R_i), 2.16 and 0.62 μA cm^{-2}, respectively. In contrast, samples Cu-Al-Ni-1.5Sn and Cu-Al-Ni SMAs had the highest R_i values, 2.56 and 3.19 μA cm^{-2}, respectively. This can be due to formation of an oxide/hydroxide film on the alloy surface, which acts as a protective layer,

thus decreasing the current density.[62] Tsao *et al.*[63] showed that the E_{corr} of Cu$_3$Sn, Cu$_6$Sn$_5$, and Cu were -311, -465, and -192 mV$_{SCE}$, respectively. Therefore, it can be inferred that secondary phases such as Cu$_3$Sn and Cu$_6$Sn$_5$ are more reactive than that of Cu. In this case, the secondary phases corroded faster compared with the Cu. Therefore, in the galvanic cell couple Cu$_3$Sn, Cu$_6$Sn$_5$ acts as the anode and Cu is the cathode. Furthermore, the density of porosity is playing a significant role in controlling the corrosion rate, in which can also described the highest corrosion resistance in Cu-Al-Ni-1 wt pct Sn SMA. This is can be attributed to the larger surface area exposed to the electrolyte compared to nonporous materials.[64] For the samples with a lower porosity, the majority of the pores are the

middle pores and small pores, which are unlikely to have trapped appreciable volumes of solution. This causes the samples relative resistance to induce corrosion. When the porosity increases as shown in Cu-Al-Ni-1.5 wt pct Sn SMA, the interconnectivity of the larger pores is markedly improved. The interconnected channels allow the free flow of the liquid and fewer sites are available to induce corrosion. From the electrochemical parameters i_{corr}, cathodic Tafel slopes (β_c), anodic Tafel slopes (β_a) of the specimens, the polarization resistance (R_P) was calculated according to the following equation:[65]

$$R_P = \frac{\beta_a \beta_c}{2.3 \ (\beta_a + \beta_c) \, i_{corr}}.$$ [6]

The corrosion resistance of Cu-Al-Ni SMA increases after addition of 0.5 wt pct Sn to the ternary SMA. All of the quaternary SMAs have a higher R_P than that of the ternary SMA. It is also obvious from the PDP curve that Cu-Al-Ni-1 wt pct Sn SMA has the highest R_P (19.20 kΩ cm^2) and Cu-Al-Ni SMA has the lowest R_P (2.97 kΩ cm^2). Furthermore, from Table IV it can be seen that the β_c increased with Sn content up to 1 wt pct from -275 to -156 mV/dec, indicating the greater difficulty of the cathodic reaction kinetics. In this regard, it has been reported[66] that β_c is around 60 and 120 mV$_{SCE}$/dec for a single-electron reaction and a double-electron reaction, respectively. The β_a increased with Sn addition from 210 to 290 mV$_{SCE}$/dec, implying that formation of the barrier oxide film made the electron transfer more difficult from the anodic site.

Figure 10 shows SEM micrographs of the ternary and quaternary SMAs after the immersion test in 3.5 pct NaCl solution. By the naked eye, the entire surfaces of Cu-Al-Ni and Cu-Al-Ni-1.5 wt pct Sn SMAs samples were severely corroded in the NaCl solution, and hence the whole of these samples was damaged. However, Cu-Al-Ni-0.5 wt pct Sn and Cu-Al-Ni-1 wt pct Sn experienced milder corrosion attack and presented a crack only. It can also be seen that the corrosion product in the SMA containing 1.5 wt pct Sn and base SMA was much thicker than the SMAs containing 0.5 and 1 wt pct Sn (Figures 10(b) and (c)). In this case, it was found that the growth mechanism of the oxide layer showed selective copper dissolution, such as a decuprification process.[59] Formation of a thick corrosion product further confirmed that the SMA containing 1.5 wt pct Sn corroded more severely compared with SMAs containing 0.5 and 1 wt pct Sn. The presence of deep and large cracks in the corrosion layer in Cu-Al-Ni-1.5 wt pct Sn can also be observed, caused by greater infiltration of the corrosive species to the SMAs (Figure 10(d)). The EDS analysis further confirmed that the corrosion product was composed of a large amount of O and Cl, accompanied by Cu, Ni, Al, and Sn (Point 1). The presence of large amounts of Cu (Point 2) showed the formation of copper compounds in the form of oxide or chloride. In general, formation of a compact oxides layer containing Ni, Cu, and Al, which is tightly bound to the substrate, can effectively protect the alloy and thus enhance its corrosion resistance. The main

reason for the higher corrosion resistance of the SMA containing Sn is the composition of the protective film formed on the SMA surface.[67] It is believed that the presence of Cu, Ni, and Al together with Sn decreases the corrosion rate of the SMA. When Cu-based alloy specimens were exposed to the NaCl solution, the cathodic reaction occurred as the following reaction:[63]

$$O_2 + 2H_2O + 4e^- \rightarrow 4OH^-.$$
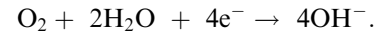
However, the anodic reaction that resulted in the copper dissolution occurred according to the following equation:[67]

$$Cu + 2Cl^- \rightarrow [CuCl_2]^- + e^-.$$
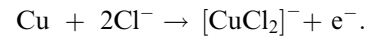
The presence of $[CuCl_2]^-$ at the surface of the SMA caused a hydrolysis reaction and the formation of Cu_2O according to the following equation:[67]

$$2[CuCl_2]^- + H_2O \rightarrow Cu_2O + 4Cl^- + 2H^+.$$

In the ternary Cu-Al-Ni SMA, aluminum oxide is formed due to the surface dissolution of aluminum according to the following equation:[67]

$$Al + 4Cl^- \rightarrow [AlCl_4]^- + 3e^-,$$

$$[AlCl_4]^- + 3H_2O \rightarrow Al_2O_3 + 6H^+ + 8Cl^-.$$
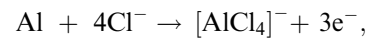
In the Sn-containing SMAs, a tin oxide film formed according to the following reaction:[63]

$$3Sn + 4OH^- + 2Cl^- - 6e^- \rightarrow Sn_3O(OH)_2Cl_2 + H_2O.$$
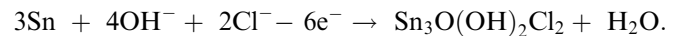
Robbiola et al.[59] demonstrated that the corrosion products of Cu-10Sn alloy immersed in NaCl solution contain $Sn_4(OH)_6Cl_2$, $Sn(OH)Cl \cdot xH_2O$, or $Sn_{21}Cl_{16}(OH)_{14}O_6$, which are a kind of tin chloride hydroxide. However, Sidot et al.[68] showed that a protective film containing tin hydroxyl/hydrated sulfate oxide may be formed on the surface of Cu-10 wt pct Sn alloy in Na_2SO_4 solution. In the case of Cu-Al-Ni-Sn SMAs, formation of a corrosion product film containing tin oxyhydroxide, aluminum dihydroxychloride and copper chloride can significantly increase the corrosion resistance of the SMA.

IV. CONCLUSIONS

A Cu-Al-Ni-xSn SMA with a particle size of 40 to 50 μm was successfully prepared by PM using mechanical alloying followed by microwave sintering. The modified alloys showed significant improvements in terms of porosity, phase-transformation temperature, mechanical properties, and corrosion behavior after the addition of Sn. The homogenized Cu-Al-Ni-xSn SMAs were formed with a fully martensite phase containing a combination

of γ_1' and β_1' martensite associated with the formation of different kinds of precipitates. In addition, the volume fraction and size of these precipitates varied based on the amount of Sn addition, in which the highest volume fraction was indicated with the addition of 1.5 wt pct of Sn. The incorporation of Cu-Al-Ni SMA with Sn has also exhibited an improvement in the transformation characteristics, which leads to the proposal of these alloys for high-temperature applications. The results of the mechanical testing showed that the highest ductility, number of cycles, and strain recovery were demonstrated in the Cu-Al-Ni-1Sn SMA, which may be attributed to the lowest porosity density and finest particle size. However, the highest strength was observed with Cu-Al-Ni-1.5 wt pct Sn because of the highest volume fraction of precipitates, which act to restrict the motion of dislocations/phase interfaces and makes the deformation more complicated. The overall corrosion behavior of ternary and quaternary SMAs significantly depended on the corrosion product film. It was found that the corrosion layer formed on the surface of Cu-Al-Ni-1.0 wt pct Sn SMA had better protective property than that of other SMAs.

ACKNOWLEDGMENT

REFERENCES

1. C. Lexcellent: *Shape-Memory Alloys Handbook*, Wiley, London, 2013.
2. K. Otsuka and C.M. Wayman: *Shape Memory Materials*, Cambridge University Press, Cambridge, 1999.
3. J. San-Juan, R.B. Pérez-Sáez, P.P. Rodríguez, M.L. Nó, and V. Recarte: in *Materials Development and Processing—Bulk Amorphous Materials, Undercooling and Powder Metallurgy*, Wiley, 2006, pp. 369–74.
4. A. Ibarra, J. San-Juan, E.H. Bocanegra, and M.L. Nó: *Mater. Sci. Eng. A*, 2006, vols. 438–440, pp. 782–86.
5. V. Recarte, J.I. Pérez-Landazábal, M.L. Nó, and J. San-Juan: *Mater. Sci. Eng. A*, 2004, vol. 370, pp. 488–91.
6. J. Font, E. Cesari, J. Muntasell, and J. Pons: *Mater. Sci. Eng. A*, 2003, vol. 354, pp. 207–11.
7. J.I. Pérez-Landazábal, V. Recarte, V. Sánchez-Alarcos, M.L. Nó, and J. San Juan: *Mater. Sci. Eng. A* 2006, vol. 438–440, pp. 734–37.
8. S.N. Saud, E. Hamzah, T. Abubakar, H.R. Bakhsheshi-Rad, M. Zamri, and M. Tanemura: *J. Mater. Eng. Perform.*, 2014, vol. 23, pp. 3620–29.
9. C.E. Sobrero, P. La Roca, A. Roatta, R.E. Bolmaro, and J. Malarría: *Mater. Sci. Eng. A*, 2012, vol. 536, pp. 207–15.
10. F. Gao, H. Song, P. Xu, M. Xie, and J. Mao: *Adv. Mater. Res.* 2011, vol. 197–198, pp. 1258–62.
11. U. Sari: *Int. J. Miner. Metall. Mater.*, 2010, vol. 17, pp. 192–98.
12. V. Sampath: *Smart Mater. Struct.*, 2005, vol. 14, pp. S253–60.
13. S.K. Vajpai, R.K. Dube, and S. Sangal: *Mater. Sci. Eng. A*, 2011, vol. 529, pp. 378–87.
14. J. Ma, I. Karaman, and R.D. Noebe: *Int. Mater. Rev.*, 2010, vol. 55, pp. 257–315.
15. S.W. Husain and P.C. Clapp: *J. Mater. Sci.*, 1987, vol. 22, pp. 2351–56.
16. S. Miyazaki, K. Otsuka, H. Sakamoto, and K. Shimizu: *Trans. Jpn Inst. Met.*, 1981, vol. 22, pp. 244–52.
17. Z. Xiao, Z. Li, M. Fang, S. Xiong, X. Sheng, and M. Zhou: *Mater. Sci. Eng. A*, 2008, vol. 488, pp. 266–72.
18. C.Y. Chung, W.G. Liu, and S.M. Tang: *J. Mater. Process. Technol.*, 1997, vol. 63, pp. 307–12.
19. C. Suryanarayana: *Prog. Mater Sci.*, 2001, vol. 46, pp. 1–184.
20. L. Wei, L. Yang, B. Yan, W.-h. Huang, and L. Bin: *J. Alloy. Compd.*, 2006, vol. 413, pp. 85–89.
21. I. Manna, P.P. Chattopadhyay, F. Banhart, and H.J. Fecht: *Mater. Lett.*, 2004, vol. 58, pp. 403–07.
22. S. Pourkhorshidi, N. Parvin, M.S. Kenevisi, M. Naeimi, and H.E. Khaniki: *Mater. Sci. Eng. A*, 2012, vol. 556, pp. 658–63.
23. S.K. Vajpai, R.K. Dube, and S. Sangal: *Mater. Sci. Eng. A*, 2013, vol. 570, pp. 32–42.
24. R.A. Portier, P. Ochin, A. Pasko, G. E. Monastyrsky, A.V. Gilchuk, V.I. Kolomytsev, and Y.N. Koval: *J. Alloys Compd.* 2013, vol. 577, pp. S472–77.
25. M. Oghbaei and O. Mirzaee: *J. Alloy. Compd.*, 2010, vol. 494, pp. 175–89.
26. S. Das, A.K. Mukhopadhyay, S. Datta, and D. Basu: *Bull. Mater. Sci.*, 2009, vol. 32, pp. 1–13.
27. J.L. Xu, L.Z. Bao, A.H. Liu, X.F. Jin, J.M. Luo, Z.C. Zhong, and Y.F. Zheng: *J. Alloy. Compd.*, 2015, vol. 645, pp. 137–42.
28. X. Rao, C.L. Chu, and Y.Y. Zheng: *J. Mech. Behav. Biomed. Mater.*, 2014, vol. 34, pp. 27–36.
29. Y.-w. Kim, K.-c. Choi, Y.-s. Chung, E. Choi, and T.-h. Nam: *J. Alloy. Compd.*, 2013, vol. 577 (Supplement 1), pp. S227–31.
30. G.K. Williamson and W.H. Hall: *Acta Metall.*, 1953, vol. 1, pp. 22–31.
31. A.S. Jabur, J.T. Al-Haidary, and E.S. Al-Hasani, *J. Alloy. Compd.* 2013, vol. 578, pp. 136–42.
32. A. Inoue, W. Zhang, T. Zhang, and K. Kurosaka: *Acta Mater.*, 2001, vol. 49, pp. 2645–52.
33. N. Saunders and A.P. Miodownik: *Bull. Alloy Phase Diagr.*, 1990, vol. 11, pp. 278–87.
34. S.N. Saud, E. Hamzah, T. Abubakar, S.N. Saud, E. Hamzah, T. Abubakar, M. Zamri, and M. Tanemura: *J. Therm. Anal. Calorim.*, 2014, vol. 118, pp. 111–12.
35. Y. Aydogdu, A. Aydogdu, and O. Adiguzel: *J. Mater. Process. Technol.*, 2002, vol. 123, pp. 498–500.
36. K. Otsuka, T. Nakamura, and K. Shimizu: *Trans. Jpn. Inst. Met.*, 1974, vol. 15, pp. 200–10.
37. K. Otsuka, T. Nakamura, and K. Shimizu: *Trans. Jpn. Inst. Met.*, 1974, vol. 15, pp. 200–10.
38. T. Ogura, S. Hirosawa, A. Hirose, and T. Sato: *Mater. Trans.*, 2011, vol. 52, pp. 900–05.
39. F.C. Lovey and E. Cesari: *Mater. Sci. Eng. A*, 1990, vol. 129, pp. 127–33.
40. F.C. Lovey, V. Torra, A. Isalgue, D. Roqueta, and M. Sade: *Acta Metall. Mater.*, 1994, vol. 42, pp. 453–60.
41. P. Franke and D. Neuschütz: in *Binary systems. Part 3: Binary Systems from Cs-K to Mg-Zr*, P. Franke and Neuschütz D. ed., Springer, Berlin, 2005, pp. 1–4.
42. T. Hoshino, N. Papanikolaou, R. Zeller, P.H. Dederichs, M. Asato, T. Asada, and N. Stefanou: *Comput. Mater. Sci.*, 1999, vol. 14, pp. 56–61.
43. N. Papanikolaou, R. Zeller, P.H. Dederichs, and N. Stefanou: *Phys. Rev. B*, 1997, vol. 55, p. 4157.
44. G.A. López, M. Barrado, J.M. San-Juan, and M.L. Nó: *Mater. Sci. Eng. A*, 2008, vol. 495, pp. 304–09.
45. V. Recarte, J.I. Pérez-Landazábal, A. Ibarra, M.L. Nó, and J. San-Juan: *Mater. Sci. Eng. A*, 2004, vol. 378, pp. 238–42.
46. V. Recarte, R.B. Pérez-Sáez, J. San-Juan, E.H. Bocanegra, and M.L. Nó: *Metall. Mater. Trans. A*, 2002, vol. 33, pp. 2581–91.
47. S.N. Saud, E. Hamzah, T. Abubakar, and H.R. Bakhsheshi-Rad: *J. Therm. Anal. Calorim.*, 2015, vol. 119, pp. 1273–84.
48. V.V. Martynov and V.V. Kokorin: *J. Phys. III*, 1992, vol. 2, pp. 739–49.
49. W.H. Wang, Z.H. Liu, J. Zhang, J.L. Chen, G.H. Wu, W.S. Zhan, T.S. Chin, G.H. Wen, and X.X. Zhang: *Phys. Rev. B*, 2002, vol. 66, p. 052411.
50. S. Jiang, Y. Zhao, Y. Zhang, L Hu, and Y. Liang, *Chin J. Nonferr. Met.* 2015, vol. 23.

51. M.S. Shakeri, J. Khalil-Allafi, V. Abbasi-Chianeh, and A. Ghabchi: *J. Alloy. Compd.*, 2009, vol. 485, pp. 320–23.
52. Z. Wang, X.-f. Liu, and J.-x. Xie: *Prog. Nat Sci.*, 2011, vol. 21, pp. 368–74.
53. N. Zárubová, A. Gemperle, and V. Novák: *Mater. Sci. Eng. A*, 1997, vol. 222, pp. 166–74.
54. J. Chen, Z. Li, and Y.Y. Zhao: *J. Alloy. Compd.*, 2009, vol. 480, pp. 481–84.
55. J. Dutkiewicz, J. Pons, and E. Cesari: *Mater. Sci. Eng. A*, 1992, vol. 158, pp. 119–28.
56. I.V. Kireeva, C. Picornell, J. Pons, I.V. Kretinina, Y.I. Chumlyakov, and E. Cesari: *Acta Mater.*, 2014, vol. 68, pp. 127–39.
57. Z. Xiao, M. Fang, Z. Li, T. Xiao, and Q. Lei: *Mater. Des.*, 2014, vol. 58, pp. 451–56.
58. S.M. Tang, C.Y. Chung, and W.G. Liu: *J. Mater. Process. Technol.*, 1997, vol. 63, pp. 307–12.
59. L. Robbiola, T.T.M. Tran, P. Dubot, O. Majerus, and K. Rahmouni: *Corros. Sci.*, 2008, vol. 50, pp. 2205–15.
60. H.R. Bakhsheshi-Rad, M.H. Idris, M.R. Abdul-Kadir, A. Ourdjini, M. Medraj, M. Daroonparvar, and E. Hamzah: *Mater. Des.*, 2014, vol. 53, pp. 283–92.
61. Z. Shi, M. Liu, and A. Atrens: *Corros. Sci.*, 2010, vol. 52, pp. 579–88.
62. J. Muller, B. Laïk, and I. Guillot: *Corros. Sci.*, 2013, vol. 77, pp. 46–51.
63. L.C. Tsao and C.W. Chen: *Corros. Sci.*, 2012, vol. 63, pp. 393–98.
64. W.U. Liang, Y. He, Y. Jiang, Y. Zeng, Y. Xiao, and B. Nan: *Trans. Nonferr. Met. Soc. China*, 2014, vol. 24, pp. 3509–16.
65. S.N. Saud, E. Hamzah, T. Abubakar, and H.R. Bakhsheshi-Rad: *Mater. Corros.*, 2014, vol. 66 (6), pp. 527–34.
66. S.J. Yuan, A.M.F. Choong, and S.O. Pehkonen: *Corros. Sci.*, 2007, vol. 49, pp. 4352–85.
67. W.A. Badawy, M.M. El-Rabiei, and H. Nady: *Electrochim. Acta*, 2014, vol. 120, pp. 39–45.
68. E. Sidot, N. Souissi, L. Bousselmi, E. Triki, and L. Robbiola: *Corros. Sci.*, 2006, vol. 48, pp. 2241–57.